



Title	Experimental Study on Shear Behavior of Reinforced-Concrete Members Fully Wrapped with Large Rupture-Strain FRP Composites
Author(s)	Jirawattanasomkul, Tidarut; Dai, Jian-Guo; Zhang, Dawei; Senda, Mineo; Ueda, Tamon
Citation	Journal of Composites for Construction, 18(3) https://doi.org/10.1061/(ASCE)CC.1943-5614.0000442
Issue Date	2014-06
Doc URL	http://hdl.handle.net/2115/57348
Type	article (author version)
File Information	JRNCCENG-S-13-00127.pdf



[Instructions for use](#)

Journal of Composites for Construction

Experimental study on shear behavior of reinforced concrete members fully wrapped with large rupture strain FRP composites

--Manuscript Draft--

Manuscript Number:	
Full Title:	Experimental study on shear behavior of reinforced concrete members fully wrapped with large rupture strain FRP composites
Manuscript Region of Origin:	JAPAN
Article Type:	Technical Paper
Manuscript Classifications:	188: FRP sheets; 227: Jackets; 312: RC Shear Strengthening; 344: Shear behavior of RC
Keywords:	fiber reinforced polymer (FRP); polyethylene terephthalate (PET) fiber; large rupture strain (LRS); reinforced concrete beams; shear strength; shear deformation
Abstract:	<p>This paper presents an experimental study on the shear behavior of reinforced concrete (RC) members fully wrapped with polyethylene terephthalate (PET) fiber reinforced polymer (FRP) composites, which are a new type of FRP material characterized with a much larger rupture strain (LRS) compared to conventional FRPs (i.e., made of carbon, glass, and aramid fibers). A total of ten PET fully-wrapped RC beams, which were designed to fail in shear and with different shear-span to effective-depth ratios, transverse reinforcement ratios and shear strengthening ratios, were tested under four-point bending loads. The overall load-deflection responses and the shear deformation of the beams as well as the strain development of the transverse steel reinforcement and the FRP jackets were carefully observed. Based upon the extensive strain measurements, the shear contributions by concrete, FRP and transverse reinforcement are differentiated. It was found that the use of PET FRP composites as the jacket material of RC members can shift the mode of shear failure from a brittle one to an ideal ductile one while the ultimate state of the members is no longer caused by FRP fracture. In order to efficiently predict the shear strength of RC members wrapped by LRS FRPs, the effective strain in LRS FRPs and the degradation of concrete at the peak member shear strength must be appropriately considered.</p>
Corresponding Author:	Tidarut Jirawattanasomkul, Ph.D. Hokkaido University Sapporo, JAPAN
Corresponding Author E-Mail:	tidarut.maintenance@gmail.com
Order of Authors:	Tidarut Jirawattanasomkul, Ph.D. Jian-Guo Dai, Ph.D. Dawei Zhang, Ph.D. Mineo Senda, M.Eng. Tamon Ueda, Ph.D.
Suggested Reviewers:	<p>Alper Ilki, Ph.D. Professor, Istanbul Technical University, Turkey ailki@itu.edu.tr He is a leading expert in the field of seismic strengthening of RC structures. He has published several relevant papers including: Goksu, C., Polat, A., and Ilki, A. "Attempt for Seismic Retrofit of Existing Substandard RC Members under Reversed Cyclic Flexural Effects." Journal of Composites for Construction, 16(3), 286-299.</p> <p>Jian-Fei Chen, Ph.D. Professor, Queen's University Belfast, U.K j.chen@qub.ac.uk He is a leading expert in the field of FRP strengthening of RC structures and has research experience in the behavior and modeling of FRP-strengthened concrete structures. He has published several relevant papers including: Cao, S. Y., Chen, J. F.,</p>

	<p>Teng, J. G., Hao, Z., and Chen, J. (2005). "Debonding in RC beams shear strengthened with complete FRP wraps." <i>Journal of Composites for Construction</i>, 9(5), 417-428.</p> <p>Thanasis C. Triantafillou, Ph.D. Professor and Director of the Structural Materials Laboratory, University of Patras, Greece ttriant@upatras.gr He is a leading expert in the field of the application of advanced structural materials in structures, with emphasis in the field of strengthening/seismic retrofitting of RC structures. He has received "best research paper of the year" award from the ASCE of Composites for Construction (2002, 2003).</p>
Opposed Reviewers:	
Additional Information:	
Question	Response
Is the article being considered for more than one journal?The Journal of Composites for Construction does not review manuscripts that are being submitted simultaneously to another organization or ASCE journal for publication.	No.
Is this article already published? Material that has been previously published cannot be considered for publication by ASCE. A manuscript that has been published in a conference proceedings may be reviewed for publication only if it has been significantly revised. If you answer YES, please provide further explanation in your cover letter.	No.
Have all the authors contributed to the study and approved the final version?All authors must have contributed to the study, seen the final draft of the manuscript, and accept responsibility for its contents. It is unethical to list someone as a coauthor who does not want to be associated with the study and who has never seen the manuscript.	Yes.
Was an earlier version of the paper previously considered and declined by ASCE?Declined manuscripts are sent through the review process again. If your manuscript has been submitted to us before under a different title, please provide that title in the space provided below. It is our policy to inform an editor that a manuscript has been previously reviewed, even when it has been reviewed by a different Division, Institute, or Council within ASCE.	No.
Do your table titles/figure captions cite other sources?If you used a figure/table from another source, written permission for print and online use must be attached in PDF format. Permission letters must state that permission is granted in both forms of media. If you used data from another source to create your own	No.

figure/table, the data is adapted and therefore obtaining permission is not required.	
Does your paper exceed 10,000 words? If YES, please provide justification in your cover letter. If you need help estimating word length, see our sizing worksheet at this link: Sizing Worksheet	Yes, I have already provided the justification in the cover letter for your kind consideration.
Estimates for color figures in the printed journal begin at \$924. Cost increases depend on the number and size of figures. Do you intend for any figure to be printed in color? If YES, how many and which ones? Please provide a total count and also list them by figure number.	No.
Is this manuscript a companion to one already submitted/or being submitted? If yes, please note whether this is part I, II, or III. Please make sure all related papers are uploaded on the same day and provide the date of submission, title, and authors of each.	No.
Is this manuscript part of a Special Issue? If yes, please provide Special Issue title and name of the guest editor.	Yes, it is a Special Issue: IIFC 10th Anniversary Issue with Guest Editors: S.T. Smith and J.F. Chen.
Journal of Composites for Construction Preview is ASCE's initiative to publish author manuscripts online within 72 hours of acceptance and before the final, copyedited version of record is published in print and online. Note: Once the manuscript is posted online, it is considered published. Edits will ONLY be allowed when the corresponding author receives a proof of the composed and copyedited version of the manuscript. Your uncopyedited manuscript will be posted online unless you click the Opt-Out button below. For more information & policy: http://pubs.asce.org/journals/pap/	Opt-In (post my uncopyedited manuscript online)
To read ASCE's Data Sharing Policy, please click on the "Instructions" link associated with this question. According to this policy, you are required to report on any materials sharing restrictions in your cover letter. Are you restricted from sharing your data & materials? If yes, did you report on these in your cover letter?	No.

1 Submission to the Special Issue of Journal of Composites for Construction on the 10th
2 Anniversary of IIFC

3

4 Experimental study on shear behavior of reinforced concrete
5 members fully wrapped with large rupture strain FRP composites

6 Tidarut Jirawattanasomkul⁽¹⁾, Jian-Guo Dai⁽²⁾, Dawei Zhang⁽³⁾, Mineo Senda⁽⁴⁾, Tamon Ueda⁽⁵⁾

7

8

9

10

11

12 (1) PhD Candidate, Division of Engineering and Policy for Sustainable Environment, Graduate School of
13 Engineering, Hokkaido University, Kita 13 Jo Nishi 8 Chome Kita-ku, Sapporo, Japan, 060-8628.
14 Email:tidarut.maintenance@gmail.com (corresponding author)

15 (2) Assistant Professor, Department of Civil and Environmental Engineering, The Hong Kong Polytechnic
16 University, Hung Hom, Kowloon, Hong Kong. Email:cejgdai@polyu.edu.hk

17 (3) Associate Professor, Department of Civil Engineering, College of Civil Engineering and Architecture, Zhejiang
18 University, Hangzhou, China, 310058. Email: dwzhang@zju.edu.cn

19 (4) Former Master Student, Division of Built Environment, Faculty of Engineering, Hokkaido University, Kita 13
20 Jo Nishi 8 Chome Kita-ku, Sapporo, Japan, 060-8628.

21 (5) Professor, Division of Engineering and Policy for Sustainable Environment, Faculty of Engineering, Hokkaido
22 University, Kita 13 Jo Nishi 8 Chome Kita-ku, Sapporo, Japan, 060-8628. Email: ueda@eng.hokudai.ac.jp

23

24 **Abstract:** This paper presents an experimental study on the shear behavior of reinforced concrete (RC)
25 members fully wrapped with polyethylene terephthalate (PET) fiber reinforced polymer (FRP)
26 composites, which are a new type of FRP material characterized with a much larger rupture strain (LRS)
27 compared to conventional FRPs (i.e., made of carbon, glass, and aramid fibers). A total of ten PET fully-
28 wrapped RC beams, which were designed to fail in shear and with different shear-span to effective-depth
29 ratios, transverse reinforcement ratios and shear strengthening ratios, were tested under four-point
30 bending loads. The overall load-deflection responses and the shear deformation of the beams as well as
31 the strain development of the transverse steel reinforcement and the FRP jackets were carefully observed.
32 Based upon the extensive strain measurements, the shear contributions by concrete, FRP and transverse
33 reinforcement are differentiated. It was found that the use of PET FRP composites as the jacket material
34 of RC members can shift the mode of shear failure from a brittle one to an ideal ductile one while the
35 ultimate state of the members is no longer caused by FRP fracture. In order to efficiently predict the shear
36 strength of RC members wrapped by LRS FRPs, the effective strain in LRS FRPs and the degradation of
37 concrete at the peak member shear strength must be appropriately considered.

38 **Keywords:** fiber reinforced polymer (FRP); polyethylene terephthalate (PET) fiber; large rupture strain
39 (LRS); reinforced concrete beams; shear strength; shear deformation

40 INTRODUCTION

41 Many existing reinforced concrete (RC) members built using old design codes are susceptible to
42 catastrophic collapse during a major earthquake due to their insufficient shear strength and member
43 ductility (Priestley 1994; Priestley 2000). Use of fiber reinforced polymer (FRP) composites as the
44 external bonding/jacketing material of RC members to improve their shear strength and ductility has been
45 a widely used technology because of the high strength-to-weight ratio and corrosion resistance of FRP
46 composites (Bakis et al. 2002; Karbhari and Zhao 2000). The most often used FRP composites in
47 application include carbon fiber reinforced polymer (CFRP), glass fiber reinforced polymer (GFRP), and
48 aramid fiber reinforced polymer (AFRP) composites, which are termed conventional FRPs in this paper.
49 In recent years, a new category of FRP composites, which are made of polyethylene naphthalate (PEN) or
50 polyethylene terephthalate (PET) fibers, have emerged as an alternative to conventional FRPs as the
51 strengthening materials of RC members. These FRPs have a much larger rupture strain (LRS) (usually
52 >5%) compared to conventional FRPs. Although their elastic modulus and strength are relatively low,
53 they are much cheaper than conventional FRPs (Jaquin et al. 2005; Ueda 2007; Dai and Ueda 2012). It
54 should be noted that the relatively low strength and modulus of LRS FRP can be compensated by the use
55 of a greater amount of the fiber material whereas the small rupture strain of conventional FRP cannot be
56 compensated in this way.

57 Existing tests have shown that square RC columns confined with LRS FRP composites within their
58 plastic hinge regions can significantly improve the member ductility when subjected to cyclic lateral
59 loading (Anggawidjaja et al. 2006; Dai et al. 2012) in the following ways: providing confinement to
60 concrete (Dai et al. 2011; Bai et al. 2013), restraining the buckling of longitudinal reinforcement (Bai et al.
61 2013), and compensating the shear degradation of concrete (Anggawidjaja et al. 2006, Jirawattanasomkul
62 et al. 2011). It is favorable that the failure mode of LRS FRP-confined RC columns subjected to lateral
63 shear at the ultimate state is no longer governed by the brittle rupture of FRPs, which is frequently

64 observed in conventional FRP-confined RC members and may lead to a sudden loss of the load-carrying
65 capacity (e.g., Seible et al. 1997; Sirbu et al. 2001; Iacobucci et al. 2003)

66 Theoretical models have been developed to predict the compressive stress-strain relationship of LRS
67 FRP-confined concrete under axial loading (Dai et al. 2011; Bai et al. 2013), and empirical models have
68 been developed to predict the ductility of LRS FRP-confined RC columns under combined axial and
69 lateral loading (Dai and Ueda 2012). However, it remains unclear how to predict the shear strength of
70 LRS FRP-strengthened RC members, which in turn may influence the development of their flexural
71 ductility (Jaşin et al. 2005; Jirawattanasomkul et al. 2011). The efficiency of LRS FRP composites for the
72 shear strengthening of RC members remains a concern because concrete degradation may occur before
73 the full activation of the strain capacity of LRS FRP composites. For instance, in the shear strengthening
74 design of RC members using conventional FRP composites it is specified in some existing codes to limit
75 the strain of FRP below a certain value (e.g., 0.4%), which is far below the rupture strain of LRS FRPs, to
76 prevent possible concrete degradation (FIB 2001; JSCE 2001; ACI Committee-440 2002). Obviously, the
77 above limitation on FRP is too conservative for LRS FRP-strengthened RC members, particularly when
78 RC members are fully wrapped with FRP composites and the brittle debonding failure of FRP is no
79 longer a critical concern and FRP composites can be more efficiently used. Preliminary tests have shown
80 that RC members fully wrapped with LRS FRP composites exhibit large shear deformation and no fiber
81 rupture when their peak shear strength is reached (Senda 2008), implying that the shear strength of LRS
82 FRP-strengthened RC members may be reached beyond the initiation of concrete degradation. Therefore,
83 for a good prediction of the shear strength of LRS FRP-strengthened RC members, further understanding
84 of the efficiency of LRS FRP composites and the degradation of the concrete shear contribution is
85 necessary.

86 Against the above background, this paper aims to conduct an experimental study for the first time on the
87 shear strength and deformation behavior of RC members strengthened with LRS FRP composites. Since it
88 is generally recommended to use LRS FRP composites as a jacketing material to confine RC columns for

89 shear and ductility enhancement, this paper only focuses on the shear behavior of LRS FRP fully wrapped
90 RC members.

91 EXPERIMENTAL PROGRAM

92 Details of Specimens

93 Ten simply-supported RC beams designed to fail in shear were subjected to four-point bending loads. RC
94 beams rather than RC columns as the test members allows the elimination of the effects of pull-out from
95 footings and lateral buckling of the longitudinal reinforcement, enabling more accurate shear deformation
96 measurement. Two groups of RC beams were prepared (see Table 1):

97 (1) Group 1 included a reference RC beam (SP1) and five RC beams fully wrapped with different
98 amounts of FRP composites (SP2 to SP6), all with identical longitudinal and transverse steel
99 reinforcement as the reference beam but different strengthening ratios of FRP. Each specimen had a cross
100 section of 250 mm \times 270 mm, whose corners were chamfered with a radius of 11 mm to prevent stress
101 concentration, and the shear span was 600 mm, resulting in a shear-span to effective-depth ratio of 2.50.
102 The longitudinal reinforcement and transverse steel reinforcement ratios were 2.53% and 0.17%,
103 respectively, in all the six specimens, whereas the volumetric ratio (i.e., calculated based on the nominal
104 thickness of the LRS FRP sheets) of the wrapped LRS FRP composites varied from 0.11 % to 0.45%.

105 (2) Group 2 included four RC beams (SP7 to SP10) that had different sectional dimensions and shear-
106 span to effective-depth ratios to the reference beam. This group was designed to investigate the effects of
107 the longitudinal reinforcement ratio and shear-span to effective-depth ratio. SP7, representing a deep
108 beam, had dimensions 250 mm \times 500 mm and a shear span of 1125 mm (see Table 1), whereas SP8 and
109 SP9 had dimensions of 250 mm \times 270 mm and a shear span length of 600 mm. SP10, representing a small
110 section of beam, had dimensions 100 mm \times 150 mm and a shear span of 300 mm. The specimen corners
111 were chamfered with a radius of 11 mm. SP7 and SP9 were designed to have a similar shear
112 strengthening ratio and shear-span to effective-depth ratio as SP5, whereas the longitudinal reinforcement

113 ratio was made different. SP8 had a similar shear strengthening and longitudinal reinforcement ratio as
114 SP3, whereas the shear-span to effective-depth ratio was made different. SP10 had a large spacing of
115 transverse reinforcement significantly less than that required in the JSCE-2007 specification.

116 For all strengthened specimens (SP2 to SP10), a continuous fiber sheet with the main fibers oriented in
117 the transverse direction was fully wrapped around the RC beam with an overlapping zone of length 250
118 designed to span the top side (subject to compression) of the specimens for firm anchorage.

119 Materials Used in the Experiments

120 *Concrete and steel reinforcement*

121 Two groups of specimens were cast with two batches of ready-mixed concrete with a maximum 20 mm
122 size of aggregate. At the time of testing, the cylinder concrete strengths of the first and second batches of
123 concrete were 25.3 MPa and 32.6 MPa, respectively. The longitudinal steel reinforcement and transverse
124 steel reinforcement were tested to find their tensile stress-strain relationships. The longitudinal
125 reinforcement used in the first and second groups of specimens had yield strengths 382 MPa, 360 MPa
126 and 539 MPa (see Table 2). In specimens SP1 to SP9, the transverse reinforcement had a 6 mm diameter
127 and a 350 MPa yield strength, whereas for SP10 the transverse reinforcement had a 13 mm diameter and
128 the same yield strength.

129 *LRS fiber sheets*

130 Polyethylene terephthalate (PET) dry fiber sheets (PET-600) were used in the experiments to form LRS
131 FRP composites. Flat coupon tests for PET FRP composites were conducted to determine their tensile
132 properties following the JSCE standard E541-2000 (2002). The tensile coupons sheets had a nominal
133 thickness of 0.841 mm, a length of 280 mm and a width of 13 mm. The coupon preparation followed the
134 usual wet lay-up process involving the impregnation of a large area of fiber sheet with a matrix epoxy
135 resin, which consisted of a main resin component and a hardener, with a mix ratio of 2:1 by weight. After

136 one week of curing in the laboratory environment, the hardened large PET FRP plate was cut into many
137 strips (i.e., testing coupons) with the required dimensions. Glass FRP (GFRP) tabs (25 mm long and 13
138 mm wide) were bonded to strengthen the two ends of each PET FRP coupon and to ensure uniform stress
139 transfer from the loading heads during the tensile tests, which were performed at a constant loading rate
140 equivalent to 1% strain per minute. An image measurement method was used to capture the tensile strain
141 of each PET flat coupon with a gauge length of 45 mm (Fig. 1a). The tensile stress in the PET FRP
142 composite was calculated from the tensile load on the basis of the nominal area of the fiber sheet. All six
143 coupons were tested and found to fail in the central region of the specimens. Fig. 1b shows the obtained
144 tensile stress-strain relationships, showing that PET FRP composites exhibit a bilinear stress-strain
145 behavior caused by the motion of amorphous phases and by the sliding or failing of macromolecular
146 chains in PET and PET fibers (Dai et al. 2011; Lechat et al. 2011). Table 3 presents a summary of the
147 material properties of PET FRP sheets provided by the manufacturer and obtained from the present tensile
148 tests. Two different values of elastic modulus, namely the initial elastic modulus (E_1) for the first linear
149 portion of the stress-strain relation and the second-stage elastic modulus (E_2) for the second linear part are
150 given in the table, together with the strain value at the transition point (ϵ_0) between the two linear portions.

151 Test Procedures and Instrumentation

152 All the beam specimens were tested under four-point loads and carefully instrumented during the tests to
153 monitor the loads, mid-span beam deflections and strains of transverse reinforcement and PET FRP
154 composites (Fig. 2a). The locations of strain gauges and LVDTs are illustrated in Figs. 2b and 2c. The
155 strain gauges were located in the region where shear cracks are expected to occur. A network of strain
156 gauges (with a gauge length of 10 mm) were mounted on all the transverse reinforcements at a spacing of
157 80 mm. Asymmetrical loading was applied to ensure failure to occur within this span. Strain gauges were
158 also attached onto the PET FRP at one beam side within the shear span. The gauge length was also 10 mm
159 and the spacing between adjacent gauges was 55 mm. For each specimen, deformations were measured
160 using LVDTs at two supports and at mid-span.

161 Various techniques have been attempted to measure the shear deformation of RC members, including the
162 placement of LVDTs (e.g., Massone and Wallace 2004; Anggawidjaja et al. 2006), the use of
163 potentiometric extensometers for curvature and shear strain measurements (e.g., Debernardi and Taliano
164 2006), and the laser speckle method (e.g., Ueda et al. 2002). Conventional LVDT-based methods were
165 used here, as shown in Fig. 3a, for the measurement of shear deformation for the first batch of specimens
166 (i.e., SP1 to SP6). However, for the second batch of specimens, the shear deformation measurement was
167 done using a more advanced digital image correlation (DIC) method with the help of charge-coupled
168 device (CCD) cameras (Fig. 3b). This method probes cracks and shear deformation of concrete surfaces
169 with high image quality, low processing cost, and can monitor until the failure of specimens while
170 avoiding causing specimen damage (Ito et al. 2002; Qi et al. 2003). For confirmation purposes, the
171 conventional LVDT-based method was implemented in parallel with the DIC method for SP7, whereas
172 only the DIC method was implemented for specimens SP8 to SP10 after its reliability was confirmed. The
173 measurement of shear deformation focused on the plastic hinge region of the specimens, which is within
174 $1.5d$ from the loading point to the support location. This region is most likely to experience shear
175 deterioration particularly during seismic loading (Anggawidjaja et al. 2006). The frame for installing the
176 LVDTs and the grid for the calibration points in the DIC method are shown in Figs.5a and 5b,
177 respectively. In the DIC measurement, the measured region was divided into many square grids, each of
178 which had four target coordinating points A, B, C and D (Fig. 5b). In order to produce a physical picture,
179 the image was translated into the digital information of target coordinate using commercially available
180 software such as Adobe Photoshop. Based upon the digital information, the shear deformation of each
181 tested beam could be calculated.

182 RESULTS AND DISCUSSION

183 Failure Modes and Crack Patterns

184 Figure 4 shows the failure modes of specimens SP1 to SP10 presenting the sketches of the failed
185 specimens and photographs after the removal of the LRS FRP jackets. The black lines drawn on the
186 concrete surface show the locations of cracks, and the hatched areas indicate the bulges on the concrete
187 surface and spalling of concrete. Except SP6, which had the largest shear strengthening ratio (Table 1), all
188 other specimens failed in shear with clear shear deformation (i.e., no yielding of flexural reinforcement
189 was observed before the yielding of transverse steel reinforcement). The shear failure in the ultimate state
190 was mainly caused by the crushing of the concrete in the compression zone at the top of the critical
191 diagonal crack (i.e., shear compression failure). At the peak load, PET FRP composites showed no sign of
192 rupture, except in SP10. For the reference SP1, spalling of concrete cover occurred. However, in all
193 strengthened specimens the spalling of concrete was prevented by the FRP confinement. Instead, bulging
194 of PET FRP composites was seen at the top of the compression region, as indicated by the hatched areas
195 in Fig. 4.

196 The angles of major diagonal shear cracks (θ_{cr}) were evaluated both from visible shear cracks and from
197 the locations of maximum strains developed in transverse steel reinforcement and PET FRP sheets at
198 different beam sections, as shown in Fig. 4 using dashed lines. The values of these angles varied from 39°
199 to 53° to the member axis. In the first group of specimens, the reference specimen (SP1) developed two
200 major shear cracks at an angle of 45°. In the strengthened specimens SP2 to SP5, the angle of the major
201 shear cracks were slightly less than 45° ranging 44° to 39°. As the member deformation increased further,
202 partial debonding of the FRP occurred near the critical shear crack or at the edge of the beam (see Fig. 5),
203 and a loud noise was produced owing to the bulge of the concrete in the compression region. Finally, the
204 PET FRP composites at the corner locations ruptured, leading to concrete crushing and a complete
205 detachment of the FRP from the concrete substrate (Fig. 5). SP6, with a 0.45% volumetric ratio of FRP,
206 showed no major shear deformation (Fig. 4) because of a confinement effect.

207 SP8 in the second group with a relatively high shear-span to effective-depth ratio ($a/d = 3.13$) exhibited a
208 crack angle of 49° in the plastic hinge area. In SP7, whose ratio of shear reinforcement spacing to beam

209 depth is smaller than the others, showed the largest crack angle ($\theta_{cr}=53^\circ$) among all the specimens. In
210 SP10, PET FRP sheets ruptured at the moment when the diagonal shear crack penetrated to the
211 compression zone of concrete, and the major shear crack did not pass any transverse steel reinforcement
212 because of their large spacing (i.e., $s = 250$ mm); the PET FRP sheets ruptured at the shear crack locations
213 rather than the corners of the beam section owing to the significant shear stress transferred from the
214 concrete to the FRP, leading to a diagonal tension failure of the member. This is an example of a poor
215 truss mechanism by which the shear stresses were not transferred through the truss nodes, leading to
216 member collapse in a very brittle behavior.

217 Overall, apart from the case when the transverse steel reinforcement ratio is extremely low, PET FRP
218 composites prevented crack opening in the strengthened beams that leads to multiple shear cracks in the
219 shear critical zones. Fig. 5 shows the locations where the PET FRP sheets ruptured, indicating that the
220 breakage of PET FRP sheets usually started from the corner of the beam section near to the loading plate
221 (e.g., in SP4). In addition, the rupture of PET FRP sheets was observed mostly at a large shear
222 deformation level.

223 Overall Load-deflection Responses

224 The overall shear force vs. mid-span deflection responses of specimens SP1 to SP6 and SP7 to SP10 are
225 presented in Figs. 6a and 6b, respectively; the shear force (V_t) is presented using a nominal shear stress
226 (v_t) by dividing the shear force by the effective cross section (i.e., $v_t=V_t/bd$). The mid-span deflection is
227 presented by the drift ratio (δ), which is defined as the ratio of the mid-span deflection (Δ_{total}) to the shear
228 span (a).

229 The reference specimen (SP1) showed a linearly increasing portion until the peak load and a sudden drop
230 of the load-carrying capacity afterwards, indicating a typical brittle shear failure of the member. During
231 the tests of specimens SP2 to SP5 the evolution of the member's mid-span deflection was terminated at
232 the rupture of PET FRP sheets. The corners in SP5 were not well rounded, resulting in the premature

233 rupture of FRP at a corner, and subsequently a lower ultimate ductility was achieved compared to SP4.
234 For SP6, which failed in flexure, neither FRP rupture nor the decrease in shear capacity was observed
235 even at the drift ratio of 12%, at which point the test was stopped owing to the extremely large
236 deformation. It is interesting that specimens SP2 to SP5 also exhibited significant ductility although they
237 failed in shear. The nominal shear stress achieved in the peak of the linear portion of the load-deflection
238 response increased with the amount of PET fiber sheets, as did the drift ratio. This is because that, with
239 increasing strengthening ratio, the confinement provided by LRS FRP not only prevented concrete from
240 spalling off but also restrained the widening of shear cracks. The considerable ductility development
241 before the member's shear failure seems to be a unique characteristic of PET FRP-strengthened RC
242 members. In other words, the shear failure is no longer brittle.

243 In the second group, SP10 was subjected to a brittle shear failure, and exhibited a load-deflection
244 response similar to that of the reference SP1. The nominal shear strength of SP10 was the highest among
245 all the specimens mainly because it had the smallest sectional dimensions (Fig. 6b). SP7 to SP9 exhibited
246 ductile shear failure (Fig. 6b). SP7 and SP9 had similar shear-span to effective-depth ratio and
247 strengthening ratio as SP5. The difference between these three specimens was their longitudinal
248 reinforcement ratios; SP9, which had the lowest value, achieved the highest shear ductility, as shown in
249 Fig. 6b, because of its highest shear to flexural strength ratio. SP7 exhibited the smallest ductility owing
250 to its higher longitudinal reinforcement ratio, as shown in Fig. 6b. The largest sectional dimensions of
251 SP7 may also be the reason for its lower shear ductility, because concrete degradation may be faster in the
252 case of large-depth RC beams owing to the widening of concrete cracks in the web. This is also witnessed
253 by the observed crack patterns (Fig. 4). SP8 had the same longitudinal reinforcement ratio and shear
254 strengthening ratio as SP3, whereas their shear-span to effective-depth ratios were different. Both two
255 specimens maintained a constant nominal shear stress until the drift ratio of approximately 5% (Figs. 6a
256 and 6b). However, SP8 showed more ductility compared to SP3 because the former had a larger shear-
257 span to effective-depth ratio than the latter (Figs. 6a and 6b).

258 Table 4 presents a comparison between the tested shear strengths and the predicted ones based upon
259 existing design codes. The shear strengths are compared in terms of three components, which are from
260 concrete (v_c), transverse steel reinforcement (v_s) and LRS FRP sheet (v_f). Each component is computed
261 based on the existing design equations in the JSCE codes (JSCE 2001; JSCE 2007) (see Appendix). For
262 the test values, the shear stresses carried by the transverse steel reinforcement (v_{s-test}) and LRS FRP (v_{f-test})
263 are obtained from their measured strain values, and then the shear contribution of concrete (v_{c-test}) can be
264 obtained. The estimations of the contributions of the transverse steel reinforcement and LRS FRP also
265 depend on the shear crack angle (θ_{cr}) of each specimen, which is also summarized in Table 4. The
266 approaches by which the strain values of transverse steel reinforcement and LRS FRP were chosen for
267 calculation will be elaborated later. It is seen in Table 4 that generally the shear contribution of concrete is
268 underestimated while the shear contribution of LRS FRP composites is overestimated. The
269 underestimation of the concrete shear contribution is due to the conservative nature of the design
270 equations, whereas the overestimation of the FRP contribution arises because the design equation was
271 derived from the experimental data of carbon and Aramid FRPs which often show the rupture of FRP at
272 the peak load.

273 Evaluation of Shear Deformation

274 The shear deformation of tested beams was calculated based on Massone and Wallace's (2004) method.
275 As shown in Fig. 7, the undeformed rectangular shape is represented by a truss element enclosed by
276 dashed lines, whereas the deformed shape due to pure shear deformation is represented by the shaded area.
277 The total deformation corresponding to the combined flexural and shear deformations is illustrated by the
278 solid lines. In case of shear deformation without flexural effect, the center of rotation is located at the
279 centroid of the truss unit. The average shear deformation (δ_s) for a specific coordinate of the concerned
280 truss can be obtained as follows:

$$\delta_s = \frac{\sqrt{|d_1^{meas}|^2 - |l + u_2|^2} - \sqrt{|d_2^{meas}|^2 - |l + u_1|^2}}{2} - \delta_f \quad (1)$$

where d_1^{meas} and d_2^{meas} are the measured diagonal lengths of the deformed truss due to combined shear and flexural actions; u_1 and u_2 are the horizontal displacements at the top and bottom of the truss unit, respectively; and l is length of the truss unit.

The contribution of the flexural deformation (δ_f) can be attributed to the rotation of tension and compression chords, BC and AD, respectively (Fig. 7). In this study, the vertical displacements due to flexure action i.e., $\delta_{f1} = \delta_{f2} = \delta_f$ is assumed to be identical for each beam cross section and can be calculated as follows:

$$\delta_f = \alpha l \frac{u_1 - u_2}{h_1} \quad (2)$$

where: α is value describing the distance from the top of the section to the centroid of the sectional curvature distribution, and is taken as 0.5, assuming that the center of rotation is at the mid-height of the truss element; h_1 is the height of the truss unit, and l is the length of the truss unit. All the parameters used in Eqs. (1) and (2) are illustrated in Fig. 7. The values of d_1^{meas} , d_2^{meas} , u_1 and u_2 were obtained from the LVDT and DIC-based measurement methods (Figs. 3a and 3b). Shear deformation contributed to total deformation at peak load (δ_{sp}/δ_p) is also summarized in Table 4.

Figure 8 shows the relationships between the nominal shear stress (v_t) and the drift ratio due to shear deformation at the mid-span (δ_s). In the first group of specimens, SP1 shows a small value of shear drift ratio at the ultimate state. In addition, at the same loading level, its shear deformation is larger than that of other specimens, because the shear crack propagated rapidly in this reference specimen. For strengthened specimens, the shear drift ratio at the ultimate state increases significantly because PET FRP sheets restrained the widening of shear cracks, shifting the member from brittle diagonal tension failure to shear

302 compression failure. SP6 failing in flexure shows the smallest shear drift ratio because no significant
303 shear crack widening occurred. Therefore, the major deformation was contributed by the flexural effect.
304 In the second group of specimens, SP7 with the greatest depth shows a significant increase in the shear
305 deformation. SP10 failed in a very brittle manner, since all shear stresses due to concrete crack opening
306 were transferred to FRP sheets, leading to the rupture of FRP followed by the sudden loss of the shear
307 load-carrying capacity. The strain development in FRP sheet and transverse steel reinforcement will be
308 reported in the next session.

309 Strain Development in PET FRP Sheets and Transverse Steel Reinforcement

310 The strains in PET FRP sheets at the shear sides of the beams in fact were induced by two types of action:
311 (1) opening of shear cracks in concrete due to shear action, and (2) the lateral expansion of concrete in the
312 beam section due to flexure. It is difficult to differentiate these two effects through experimental
313 measurement. Taking SP2 as an example, Fig. 9 presents the typical strain distributions in PET FRP
314 sheets along the shear span (Fig. 9a) as well as along the beam height (Fig. 9b) at the peak load. For each
315 measured section (i.e., represented by a strip in Fig. 9) along the shear span, there is a maximum strain
316 observed in the FRP sheets (Fig. 9b). Most of these maximum strains were observed around a major
317 diagonal shear crack (see the dashed line in Fig. 9a) in the shear-critical region of the member. However,
318 some of them deviated somewhat from the dashed lines probably due to the existence of multi-shear
319 cracks. The high strains at the top corner of the section near the loading plate, due to the bulging of
320 concrete, result in a dilatation of the FRP sheets in the outward direction (see Figs. 4 and 9b).

321 Figure 10 shows the strain distributions in transverse steel reinforcement along the shear span and the
322 sectional depth. The strain distributions of transverse steel reinforcement in the shear-critical region are
323 similar to those of PET FRP sheets. However, the maximum strains are always observed at the mid-height
324 of the shear side of the beam (Fig. 10a) rather than the top corner because there is negligible effect of the
325 concrete bulging on the transverse steel reinforcement.

326 The locations of strain gauges bonded on FRP sheets and transverse steel reinforcement intersected with
327 the critical shear crack are also shown in Figs. 9 and 10. The readings of the strain gauges at these
328 locations (i.e., marked with circles in strips F2 to F5 in Fig. 9, and in lines S1 to S3 in Fig. 10) were
329 recorded to calculate the shear stress contribution from FRP sheets ($v_{f\text{-test}}$) and the transverse steel
330 reinforcement ($v_{s\text{-test}}$), which represent integrals of the tensile force along each strip/line.

331 Figure 11 shows the typical development of the strains in transverse steel reinforcement and PET FRP
332 sheets with the shear deformation, which is also represented by the drift ratio, until the members' ultimate
333 states. The locations where the maximum strains in both transverse steel reinforcement and PET FRP
334 sheets in all the specimens are summarized in Table 5 with reference to Figs. 2b, 2c and 2d. The average
335 strains of transverse steel reinforcement and PET FRP sheets are the average values of all strain readings
336 on the strip on which the maximum value was observed. In all the strengthened beams, the transverse
337 steel reinforcement and PET FRP sheets tended to have similar maximum strain values before the
338 yielding of the transverse steel reinforcement. An approximately linear increase of the maximum and
339 average strains with the shear deformation was seen during this period. Beyond this the strain increase in
340 transverse steel reinforcement and PET FRP sheets behaved nonlinearly. The rate of strain increase in
341 FRP sheets and transverse steel reinforcement first increased due to the stiffness degradation of the
342 transverse steel reinforcement and then decreased after the peak load (δ_{sp}). In the reference specimen, the
343 increase in strain of transverse reinforcement was, however, nearly constant after the peak load because
344 the ultimate state was reached shortly after the shear crack propagation. The strain increase in LRS FRP
345 sheets was usually larger than that in transverse steel reinforcement because of the dual effects of LRS
346 FRP sheets (i.e., shear strengthening and confinement effects).

347 The difference between the average strain and the maximum strain of FRP sheets reflects the extent of
348 strain localization. It is seen that such a difference was smaller in SP2 (Fig. 11a) than that in SP5 (Fig.
349 11b). This is mainly because the location of the maximum strain observed in SP2 was closer to the major
350 shear crack (F-18 in Table 5) while that observed in SP5 was closer to the top corner of the section. The

351 stress concentrations at the former and latter locations tended to lead to easy debonding and fiber rupture,
352 respectively.

353 Figs. 11c and 11d show the development of the maximum strain in FRP sheets and transverse steel
354 reinforcement with the shear deformation for Group 1 and Group 2 beams, respectively. For the first
355 group, just SP1 to SP4 are presented due to the premature failure of SP5 and the different failure mode of
356 SP6. It is seen that the strengthening ratio influenced significantly the strain development in both FRP
357 sheets and transverse steel reinforcement. Given the same drift ratio due to shear deformation, the higher
358 strengthening ratio of LRS FRP sheets was used, the higher strain values developed in both the FRP
359 sheets and the transverse steel reinforcement. For the second group of specimens, SP7 with the highest
360 longitudinal reinforcement ratio developed higher strain values in the FRP sheets with the shear
361 deformation compared to SP9, which had the lowest longitudinal reinforcement ratio. Strains of
362 transverse steel reinforcement in SP9 were not available due to the breakage of gauges. Compared to all
363 other specimens in Group 2, SP8 exhibited the faster strain development in the FRP sheets with the
364 deflection increase during the whole loading period owing to its largest shear-span-to-effective depth ratio
365 ($a/d = 3.13$).

366 Table 5 summarizes the maximum and average strains developed in PET FRP sheets and transverse steel
367 reinforcement, which were observed at the peak load, the defined ultimate state (i.e., corresponding to a
368 20% drop of peak load), and the termination of the test. It was not possible to define the ultimate state for
369 SP3, for which case the test was terminated before the defined ultimate state was reached, and for SP6,
370 which exhibited no drop of the peak load. In most specimens, the strain values of the transverse
371 reinforcement were not available at the termination of tests due to the large damage in concrete that broke
372 the strain gauges. The maximum strains in LRS FRP sheets were usually observed at the location either
373 close to the major shear crack or close to the one corner of the beam section. If excluding the reference
374 SP1 and SP10, which experienced diagonal tensile shear failure, the maximum strain values in LRS FRP
375 sheets in different states are: (1) 10,280-60,615 $\mu\epsilon$ at the peak loads; (2) 39,756-116,613 $\mu\epsilon$ at the defined

376 ultimate state; and (3) 15,470-139,773 $\mu\epsilon$ at the termination of tests; on the other hand, the maximum
377 strain values in transverse steel reinforcement are 5,648-16,315 $\mu\epsilon$ at the peak loads while 13,070-75,133
378 $\mu\epsilon$ at the defined ultimate state. The large strain values observed in FRP sheets also demonstrate the
379 significance of using LRS FRP sheets for maintaining the integrity and ductility of RC members at large
380 shear deformation levels.

381 Degradation of the Shear Contribution of Concrete

382 The contribution of concrete to the shear resistance can be isolated from the total member shear force
383 once the shear contributions of transverse steel reinforcement and LRS FRP sheets are known from the
384 analyses on strain readings. The shear contribution of concrete in RC members wrapped with LRS FRP
385 sheets was usually found to have reached its peak value before the full development of the member shear
386 strength, as shown in Fig. 12. For example, in SP7 the concrete contribution to shear started degrading at
387 the shear drift ratio of 0.80% while had degraded by 47.6% compared to its peak value at the shear drift
388 ratio of 2.35% (Fig. 12a). A similar phenomenon was observed in all other strengthened members such as
389 in SP10 (Fig. 12b). The extent of degradation varied from a range of 0~54.6% depending on the
390 volumetric ratio of FRP sheets, the shear-span to effective-depth ratio and the depth of member section.
391 Therefore, the prediction of the degradation of concrete shear contribution is essential for RC members
392 strengthened by LRS FRP composites.

393 Figure 13 shows the relationships between the concrete shear stress (v_c) and the member drift ratio due to
394 shear deformation (δ_s). In the first group of specimens, the maximum shear contributions from concrete
395 are different for different specimens in spite of their identical sectional dimensions because the fully
396 wrapped FRP sheets provided confinement to concrete and hence enhanced its compressive concrete
397 strength, as shown in Fig. 13a and Table 4 (v_{c-test} at peak load). In addition, the mark “x” in Figs. 13a and
398 13b indicates the shear drift ratio levels at which the member's shear strength was reached in SP4, SP7 to
399 SP10 as examples. These levels (i.e., δ_{sp}) for all other specimens can be found in Table 4. In the second

400 group of specimens, the degradation of the concrete shear contribution in SP8, which had a higher shear-
401 span to effective-depth ratio, started earlier than that in other specimens, indicating that the shear-span to
402 effective-depth ratio influenced the initiation of concrete degradation. In SP10, the concrete shear
403 degradation suddenly lost after the peak due to insufficient transverse reinforcement.

404 The shear contribution of concrete in an RC beam depends on the stiffness of both longitudinal and
405 transverse reinforcement (Sato et al. 1997). When the yielding of longitudinal reinforcement in tension
406 region takes place the stiffness of this reinforcement starts to reduce, leading to the decrease of the
407 potential shear strength of the RC beam. The yielding of longitudinal reinforcement is followed by the
408 uplifting of the neutral axis, which limits the contribution of concrete in the compression zone. The
409 change of neutral axis also increases the compression strain that accelerates the softening or crushing of
410 concrete. Similarly, the yielding of transverse reinforcement also leads to its stiffness reduction and no
411 further increase in its contribution to the member shear strength. Therefore, it is highly possible that to
412 predict the degradation in the shear contribution of concrete in LRS FRP-strengthened RC members by
413 correlating it to the strain levels of the longitudinal reinforcement and transverse reinforcing materials
414 (i.e., including both FRP sheets and transverse steel reinforcement).

415 CONCLUSIONS

416 An experimental program involving tests on ten RC beams strengthened in shear with fully wrapped LRS
417 PET FRP sheets has been conducted. The test parameters include the strengthening ratio, the longitudinal
418 reinforcement ratio as well as the shear-span to effective-depth ratio. The following conclusions can be
419 drawn from the test results:

- 420 (1) PET FRP sheets with a large rupture strain can be used to enhance the shear strength of RC beams
421 while substantially increasing the member ductility. In particular, PET FRP sheets did not rupture at
422 the peak load and led to a ductile shear failure of the strengthened RC members. This failure mode

423 also enabled us to clearly observe the behavior of shear strength degradation of concrete with the
424 increase of shear deformation until the rupture of PET FRP sheets.

425 (2) The increase of amount of PET FRP sheets led to an increase of the shear strength and shear ductility
426 whereas a lower longitudinal reinforcement ratio and a smaller shear-span to effective-depth ratio
427 corresponded to improved shear ductility.

428 (3) PET FRP sheets developed very high strains; namely the maximum strains of 1.4-6% at the peak
429 shear loads and as high as 15.0% at the termination of tests,.

430 (4) The initiation of the degradation of the shear contribution of concrete occurred even before the peak
431 strength was developed in PET FRP-strengthened RC members. The shear contribution of concrete
432 was found to degrade by 0-54.6% depending on the volumetric ratio of FRP sheets, the shear-span to
433 effective-depth ratio and the member depth. This degradation of concrete contribution to shear
434 strength is eligible in the case of no axial loading for the current study.

435 Due to the close relationships among the concrete shear deterioration, the member shear deformation and
436 the strain levels in the transverse reinforcing materials including both FRP sheets and transverse steel
437 reinforcement as observed in the current experimental study, further research work should be carried out
438 to build up a comprehensive model to explain the above relationships. The development of such a
439 comprehensive model is being reported by the authors and the improvement of the shear strength model
440 by the authors (Jirawattanasomkul et al. 2011) will be reported shortly.

441 Acknowledgements

442 The authors would like to acknowledge Mr Hiroshi Nakai of Maeda Kosen Co. Ltd, Japan, for providing
443 invaluable advice to this study and the Aramid Reinforcement Association, Japan, for providing epoxy
444 resins and PET fiber sheets for this study. The authors are also grateful to the financial aid provided by
445 the Grant-in-Aid for Scientific Research (A) in Japan (Project code: 22246058) and the collaboration
446 opportunity provided by The Hong Kong Polytechnic University through the National Natural Science
447 Foundation of China (Project code: 51172146).

448 Appendix: Calculation of shear contribution

449 According to JSCE specifications (JSCE 2001, JSCE 2007), total shear strength (v_t) consists of the
 450 contribution to shear strength due to concrete (v_c), transverse steel reinforcement (v_s) and FRP sheet (v_f).

$$451 \quad v_t = v_c + v_s + v_f \quad (3)$$

452 The concrete and transverse steel contributions to shear strength can be calculated as follows:

$$453 \quad v_c = 0.20 \cdot \sqrt[3]{f'_c} \cdot \sqrt[4]{1000/d} \cdot \sqrt[4]{100\rho_w} \quad (4)$$

$$454 \quad v_s = \left[A_w f_{wy} (\sin \alpha_s + \cos \alpha_s) / s_s \right] \cdot z / (bd) \quad (5)$$

455 where f'_c is compressive strength of concrete; b is width of member, d is effective depth of member; ρ_w
 456 is ratio of transverse steel reinforcement; A_w is cross-sectional area of transverse steel reinforcement; f_{wy} is
 457 yielding strength of transverse reinforcement; α_s is angle of transverse steel reinforcement to the
 458 member's axis; and z is $d/1.15$.

459 The shear contribution due to FRP sheet comes from the capacity of FRP sheet to carry tensile stress from
 460 the developed strain. The nominal shear strength is computed based on the coefficient expressing the
 461 shear reinforcing efficiency of the continuous fiber sheet (K) as shown in Eq. (6). This coefficient
 462 represents the strain of FRP at breakage which varies from 0.4 to 0.8.

$$463 \quad v_f = K \cdot \left[A_f f_{fu} (\sin \alpha_f + \cos \alpha_f) / s_f \right] \cdot z / (bd) \quad (6)$$

464 where $K = 1.68 - 0.67R$ in which $0.4 \leq K \leq 0.8$ and $R = (\rho_f E_f)^{1/4} (f_{fu} / E_f)^{2/3} (1 / f'_c)^{1/3}$ in which
 465 $0.5 \leq R \leq 2.0$; A_f is cross-sectional area of continuous FRP sheets; f_{fu} is design tensile strength of
 466 continuous fiber sheet (N/mm^2); s_f is spacing of continuous FRP sheet; E_f is modulus of elasticity of

467 continuous FRP (kN/mm^2); ρ_f is volumetric ratio of FRP sheet; and α_f is angle formed by continuous FRP
468 sheet to the member axis.

469 References

470 ACI Committee 440. (2002). Guide for the Design and Construction of Externally Bonded FRP Systems
471 for Strengthening Concrete Structures, American Concrete Institute, Farmington Hills, MI, USA.

472 Anggawidjaja, D., Ueda, T., Dai, J., and Nakai, H. (2006). "Deformation capacity of RC piers wrapped by
473 new fiber-reinforced polymer with large fracture strain." *Cement and Concrete Composites*, 28(10),
474 914-927.

475 Bai, Y.L., Dai, J.G. and Teng, J.G. (2013). "Cyclic compressive behavior of concrete confined with large
476 rupture strain FRP composites." *Journal of Composites for Construction*, ASCE (Accepted for
477 publications)

478 Bakis, C. E., Bank, L. C., Brown, V. L., Cosenza, E., Davalos, J. F., Lesko, J. J., Machida, A., Rizkalla, S.
479 H., and Triantafillou, T. C. (2002). "Fiber-reinforced polymer composites for construction-state-of-
480 the-art review." *Journal of Composites for Construction*, ASCE, 6(2), 73-87.

481 Dai, J. G., Bai, Y.L. and Teng, J.G. (2011), "Behavior and modeling of concrete confined with FRP
482 composites of large deformability." *Journal of Composites for Construction*, ASCE, 15(6), 963-973.

483 Dai, J.G., Lam, L., and Ueda, T. (2012). "Seismic retrofit of square RC columns with polyethylene
484 terephthalate (PET) fibre reinforced polymer composites." *Construction and Building Materials*, 27(1),
485 206-217.

486 Dai, J. G. and Ueda, T. (2012). "Strength and deformability of concrete members wrapped with fibre
487 reinforced polymer composites with a large rupture strain." *Innovative Materials and Techniques in
488 Concrete Construction*, ISBN 978-94-007-1996-5, Edited by Fardis Michael N., Springer Publisher,
489 Chapter 14, 225-241.

490 Debernardi, P. G., and Taliano, M. (2006). "Shear deformation in reinforced concrete beams with thin
491 web." *Magazine of Concrete Research*, 58(3), 157-171.

- 492 FIB. (2001). Externally Bonded FRP Reinforcement for RC Structures, The International Federation for
493 Structural Concrete, Lausanne, Switzerland.
- 494 Iacobucci, R. D., Sheikh, S. A., and Bayrak, O. (2003). "Retrofit of square concrete columns with carbon
495 fiber-reinforced polymer for seismic resistance." *ACI Structural Journal*, 100(6), 785-794.
- 496 Ito, A., Aoki, Y., and Hashimoto, S. (2002). "Accurate extraction and measurement of fine cracks from
497 concrete block surface image." *Proceeding of 28th Annual Conference of the Industrial Electronics*
498 *Society*, Industrial Electronics Society, 3(1), 2202-2207.
- 499 Japan Society of Civil Engineers JSCE. (2001). "Recommendations for upgrading of concrete structures
500 with use of continuous fiber sheets." Concrete Engineering Series Rep., Committee 292 on Concrete
501 Structures with Externally Bonded Continuous Fiber Reinforcing Materials, Tokyo, 41.
- 502 Japan Society of Civil Engineers (JSCE). (2002). "Test method for tensile properties of continuous fiber
503 sheets." Japan Society of Civil Engineers, JSCE-E541-2000.
- 504 Japan Society of Civil Engineers (JSCE). (2007). "Standard specification for concrete structures -
505 structural performance verification - design." Series 2007(15), Tokyo.
- 506 Jaqin, H., Nakai, H., Ueda, T., Sato Y., and Dai, J. (2005). "Seismic retrofitting of RC piers using
507 continuous fiber sheet with large fracturing strain." *Journal of Structural Engineering*, JSCE, 51A ,
508 893-902.
- 509 Jirawattanasomkul, T., Ikoma, Y., Zhang D., and Ueda, T. (2011) "Shear strength of reinforced concrete
510 members strengthened with FRP jacketing." *Proceedings of Japan Concrete Institute*, Japan Concrete
511 Institute, 33(2), 991-996.
- 512 Karbhari, V. M., and Zhao, L. (2000). "Use of composites for 21st century civil infrastructure." *Computer*
513 *Methods in Applied Mechanics and Engineering*, 185(2-4), 433-454.
- 514 Lechat, C., Bunsell, A. R., and Davies, P. (2011). "Tensile and creep behavior of polyethylene
515 terephthalate and polyethylene naphthalate fibres." *J. Material Science*, 46(2), 528-533.
- 516 Massone, L. M., and Wallace, J. W. (2004). "Load-deformation responses of slender reinforced concrete
517 walls." *ACI Structural Journal*, 101(1), 103-113.

- 518 Priestley, M. J. N., Verma, R., and Xiao, Y. (1994). "Seismic Shear Strength of Reinforced Concrete
519 Columns." *Journal of Structural Engineering*, ASCE, 120(8), 2310-2327.
- 520 Priestley, M. J. N. (2000). "Performance-based seismic design." Keynote Address, *Proceeding of 12th*
521 *World Conference on Earthquake Engineering*, Auckland, New Zealand, 1-22.
- 522 Qi, C., Weiss, J., and Olek, J. (2003). "Characterization of plastic shrinkage cracking in fiber reinforced
523 concrete using image analysis and a modified Weibull function." *Materials and Structures*, 36(6), 386-
524 395.
- 525 Sato, Y., Ueda, T., and Kakuta, Y. (1997). "Shear strength of reinforced and prestressed concrete beams
526 with shear reinforcement." *Concrete Library International of JSCE*, No.29. 233-247.
- 527 Senda, M. and Ueda, T. (2008). "Experimental study on shear strengthening by continuous fiber with
528 high fracturing strain." *Proceedings of the Concrete Structure Scenarios*, JSMS, 8, 249-256 (in
529 Japanese).
- 530 Sirbu, G., Ueda, T., and Kakuta, Y. (2001). "A study on shear resisting mechanism of RC columns
531 strengthened with carbon fiber sheets." *Journal of Structural Engineering*, JSCE, 47(3), 1289-1298.
- 532 Seible, F., Priestley, M. J. N., Hegemier, G. A., and Innamorato, D. (1997). "Seismic retrofit of RC
533 columns with continuous carbon fiber jackets." *Journal of Composites for Construction*, ASCE, 1(2),
534 52-62.
- 535 Ueda, T., Sato, Y., Ito, T., and Nishizono, K. (2002). "Shear deformation of reinforced concrete beam."
536 *Journal of Materials, Concrete Structures, Pavements*, JSCE, 711(56), 205-215.

Table 1 Details of test specimens

Items	unit	Specimen																			
		SP1	SP2	SP3	SP4	SP5	SP6	SP7	SP8	SP9	SP10										
f_c	MPa	25.3	25.3	25.3	25.3	25.3	25.3	25.3	25.3	25.3	25.3	25.3	25.3	25.3	25.3	25.3	25.3	25.3	25.3	25.3	25.3
b	mm	250	250	250	250	250	250	250	250	250	250	250	250	250	250	250	250	250	250	250	250
h	mm	270	270	270	270	270	270	270	270	270	270	270	270	270	270	270	270	270	270	270	270
d	mm	240	240	240	240	240	240	240	240	240	240	240	240	240	240	240	240	240	240	240	240
a	mm	600	600	600	600	600	600	600	600	600	600	600	600	600	600	600	600	600	600	600	600
a/d	-	2.50	2.50	2.50	2.50	2.50	2.50	2.50	2.50	2.50	2.50	2.50	2.50	2.50	2.50	2.50	2.50	2.50	2.50	2.50	2.50
Longitudinal reinforcement in compression		←	←	←	←	←	←	←	←	←	←	←	←	←	←	←	←	←	←	←	←
Longitudinal reinforcement in tension		←	←	←	←	←	←	←	←	←	←	←	←	←	←	←	←	←	←	←	←
Transverse reinforcement		D6	D6	D6	D6	D6	D6	D6	D6	D6	D6	D6	D6	D6	D6	D6	D6	D6	D6	D6	D6
ρ_{sc}	%	2.53	2.53	2.53	2.53	2.53	2.53	2.53	2.53	2.53	2.53	2.53	2.53	2.53	2.53	2.53	2.53	2.53	2.53	2.53	2.53
ρ_{st}	%	4.22	4.22	4.22	4.22	4.22	4.22	4.22	4.22	4.22	4.22	4.22	4.22	4.22	4.22	4.22	4.22	4.22	4.22	4.22	4.22
ρ_w	%	0.17	0.17	0.17	0.17	0.17	0.17	0.17	0.17	0.17	0.17	0.17	0.17	0.17	0.17	0.17	0.17	0.17	0.17	0.17	0.17
ρ_f	%	0.00	0.11	0.17	0.22	0.34	0.45	0.34	0.34	0.45	0.34	0.34	0.17	0.17	0.34	0.17	0.17	0.34	0.17	0.34	0.19
s	mm	150	150	150	150	150	150	150	150	150	150	150	150	150	150	150	150	150	150	150	150
t_f	mm	0	0.28	0.42	0.56	0.84	1.12	0.84	0.84	1.12	0.84	0.42	0.42	0.84	0.42	0.84	0.42	0.84	0.42	0.84	0.18
A_w	mm ²	63.34	63.34	63.34	63.34	63.34	63.34	63.34	63.34	63.34	63.34	63.34	63.34	63.34	63.34	63.34	63.34	63.34	63.34	63.34	63.34
E_f	GPa	0	9.58	9.58	9.58	9.58	9.58	9.58	9.58	9.58	9.58	9.58	9.58	9.58	9.58	9.58	9.58	9.58	9.58	9.58	9.58
E_w	GPa	196	196	196	196	196	196	196	196	196	196	196	196	196	196	196	196	196	196	196	196
$E_f t_f$	KN/mm	0.00	0.34	4.02	5.36	8.05	10.73	8.05	8.05	10.73	8.05	4.02	4.02	8.05	4.02	8.05	4.02	8.05	4.02	8.05	1.72
$E_w A_w / s$	KN/mm	82.76	82.76	82.76	82.76	82.76	82.76	82.76	82.76	82.76	82.76	82.76	82.76	82.76	82.76	82.76	82.76	82.76	82.76	82.76	198.67
$E_f A_f / (E_w A_w / s)$	-	-	0.03	0.05	0.06	0.10	0.13	0.10	0.10	0.13	0.10	0.05	0.05	0.10	0.05	0.10	0.05	0.10	0.05	0.10	0.01

f_c = compressive strength of concrete cylinder; b = width of beam cross-section; h = total depth of beam cross-section; d = effective depth of beam cross-section; a/d = shear-span to effective-depth ratio; ρ_{sc} = ratio of compression reinforcement; ρ_{st} = ratio of tension reinforcement; ρ_w = ratio of transverse steel reinforcement; ρ_f = volumetric ratio of FRP sheet; s = spacing of transverse steel reinforcement; t_f = total nominal thickness of FRP sheet for both shear sides; A_w = total cross-sectional area of both legs for one single transverse steel reinforcement; E_f , E_w = Young's modulus of FRP sheet, and Young's modulus of transverse steel reinforcement.

Table 2 Material properties of steel reinforcement

Item	Diameter (mm)	Sectional area (mm²)	Yielding strength (MPa)	Young's modulus (MPa)	Yielding strain (με)
Longitudinal reinforcement					
D25 (SD345)	25	506.7	382	188,000	2,000
D25 (SD490)	25	506.7	539	198,000	2,700
D13 (SD360)	13	126.7	360	180,000	2,000
Transverse Reinforcement					
D13	13	126.7	360	180,000	2,000
D6	6	31.67	350	196,000	1,800

Table 3 Material properties of PET FRP sheets

Product	Manufacturer data					Present tensile tests				
	Nominal thickness (mm)	Tensile strength (MPa)	Young's modulus (MPa)	Rupture strain (%)	Nominal thickness (mm)	Tensile strength (MPa)	Strain at transition, ϵ_o (%)	Rupture strain (%)	E_1 (MPa)	E_2 (MPa)
PET-600	0.841	740	10,000	6.7-8.2	2.5	704	0.74	6.43	21,452	9,580

Table 4 Summary of test results in shear-stress and drift-ratio component

Items	unit	Specimen									
		SP1	SP2	SP3	SP4	SP5	SP6	SP7	SP8	SP9	SP10
Calculation at δ_p											
v_c	MPa	1.78	1.78	1.78	1.78	1.78	1.78	1.69	1.77	1.79	2.30
v_s	MPa	1.48	1.48	1.48	1.48	1.48	1.48	1.58	1.85	1.48	1.85
v_f	MPa	-	0.27	0.41	0.55	0.82	1.10	0.82	0.41	0.82	0.44
v_l	MPa	3.26	3.53	3.67	3.80	4.08	4.35	4.09	4.03	4.09	4.59
v_{mu}	MPa	5.58	5.58	5.58	5.58	5.58	5.58	5.94	5.75	6.25	6.11
v/v_{mu}	-	0.58	0.63	0.66	0.68	0.73	0.78	0.69	0.70	0.65	0.75
Test at δ_p											
v_{c-test}	MPa	1.86	2.59	2.25	2.78	2.45	2.30	1.05	0.75	1.35	4.40
v_{s-test}	MPa	1.12	1.06	1.11	1.11	1.11	1.14	1.11	1.19	1.19	0.99
v_{f-test}	MPa	-	0.23	0.46	0.44	0.62	1.00	1.73	1.29	1.72	0.28
v_{l-test}	MPa	2.97	3.87	3.82	4.33	4.14	4.43	3.89	3.22	4.26	5.68
δ_p	%	0.66	0.95	0.80	1.39	1.14	11.44	2.61	4.28	9.96	1.64
δ_{sp}	%	0.48	0.23	0.16	0.42	0.22	0.91	2.35	2.70	6.13	0.62
δ_{sp}/δ_p	-	0.73	0.24	0.20	0.30	0.19	0.08	0.90	0.63	0.62	0.38
Test at δ_u^*											
v_{c-test}	MPa	1.33	1.60	-	0.34	1.49	-	0.48	0.47	0.45	2.90
v_{s-test}	MPa	1.05	1.17	-	1.22	1.08	-	1.14	1.19	1.19	1.18
v_{f-test}	MPa	-	0.32	-	1.91	0.73	-	1.41	0.08	1.78	0.23
v_{l-test}	MPa	2.38	3.10	-	3.46	3.30	-	3.03	2.58	3.42	4.31
δ_u	%	0.96	3.76	-	8.46	4.06	-	6.60	5.28	12.06	2.49
At the end of test											
v_{c-test}	MPa	1.25	1.30	1.17	0.00	0.99	2.30	0.12	0.35	0.00	0.00
v_{s-test}	MPa	1.11	1.11	1.17	1.22	1.08	1.14	1.13	0.80	1.19	1.88
v_{f-test}	MPa	0.00	0.13	1.15	0.80	0.38	1.00	0.21	0.29	1.55	0.22
v_{l-test}	MPa	2.37	2.54	3.49	2.01	2.45	4.43	1.46	1.44	2.61	1.79
δ_{end}	%	1.07	4.89	5.27	11.42	6.0	11.44	8.84	9.53	13.05	8.59
Major shear crack angle (θ_{cr})											
	-	45°	44°	39°	39°	39°	N.A	53°	49°	46°	45°
Failure mode											
	-	Shear. comp	Shear. comp	Shear. comp	Shear. comp	Shear. comp	Shear. comp	Shear. comp	Shear. comp	Flexure	Diag. tens

*The ultimate state (δ_u) is defined to be reached with the load dropped by 20% compared to its peak load; Shear. comp = Shear compression failure; Diag. tens = Diagonal tension failure.

Table 5 Strain development in PET FRP sheets and transverse steel reinforcement

State	Specimen	SP1	SP2	SP3	SP4	SP5	SP6	SP7	SP8	SP9	SP10	
At peak load (δ_p)	Recorded location	-	F-18	F-18	F-18	F-17	F-18	F-39	F-25	F-16	F-4	
	FRP strain (ϵ_f)		14,612	17,450	19,370	12,830	10,280	46,340	60,615	38,970	11,040	
	Average	-	10,671	12,119	13,532	6,522	6,496	5,498	14,837	27,109	4,120	
At ultimate state (δ_u)	Recorded location	S-3	S-8	S-8	S-8	S-8	S-5	S-6	S-12	N.A	S-2	
	Transverse steel reinforcement strain (ϵ_w)		15,200	10,355	17,276	16,315	13,145	13,817	15,618	31,650	N.A	673
	Average	5,648	7,262	9,424	13,651	8,920	13,062	15,618	24,182	N.A	581	
At the end of test	Recorded location	-	F-18	F-18	F-18	F-17	F-18	F-39	F-25	F-16	F-4	
	FRP strain (ϵ_f)		45,450	-	135,719	39,756	-	116,613	73,064	49,210	7,680	
	Average	-	39,450	-	108,575	11,213	-	42,332	43,770	27,913	2,693	
At the end of test	Recorded location	S-3	S-8	S-8	S-8	S-8	S-5	S-6	S-12	N.A	S-2	
	Transverse steel reinforcement strain (ϵ_w)		15,192	29,306	-	75,133	31,029	-	13,071	38,968	N.A	829
	Average	5,635	20,816	-	75,133	16,021	-	11,571	33,119	N.A	476	
At the end of test	Maximum strain in FRP	-	58,198 (F-14)	129,616 (F-18)	99,779 (F-18)	48,783 (F-17)	15,470 (F-16)	139,773 (F-39)	147,773 (F-25)	53,231 (F-16)	6,160 (F-4)	
	Maximum strain in transverse steel	15,464 (S-3)	36,711 (S-8)	N.A	N.A	N.A	N.A	N.A	N.A	N.A	1,261 (S-2)	

*N.A Not available owing to strain gauge breakage

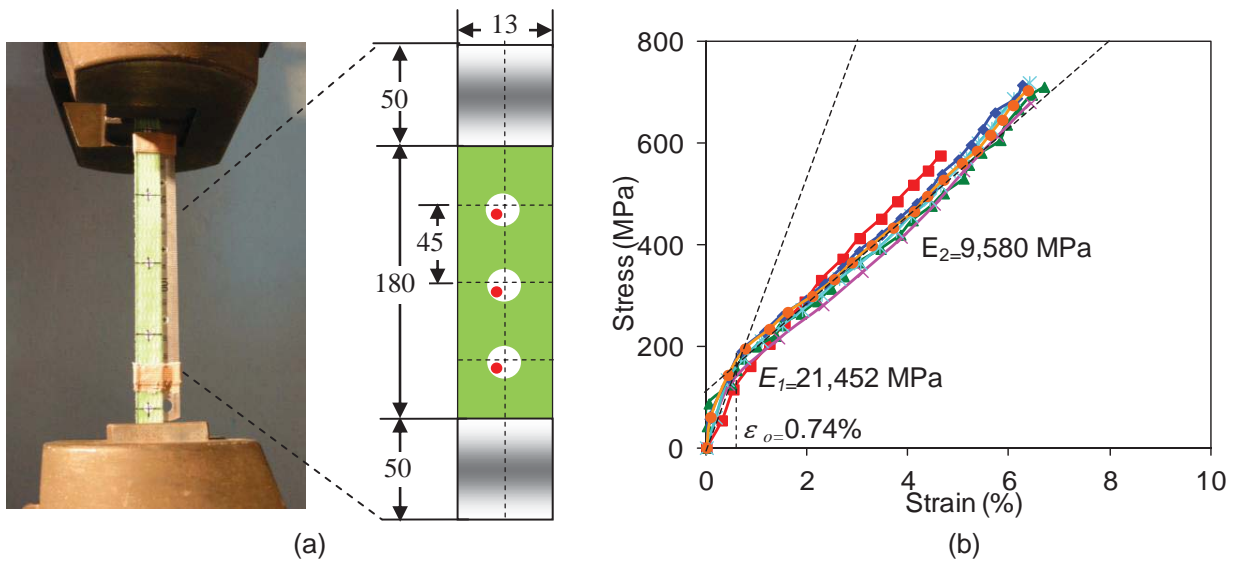


Fig. 1 Tensile test of flat coupon: (a) Tensile test and flat coupon; and (b) Stress-strain relationship of flat coupon

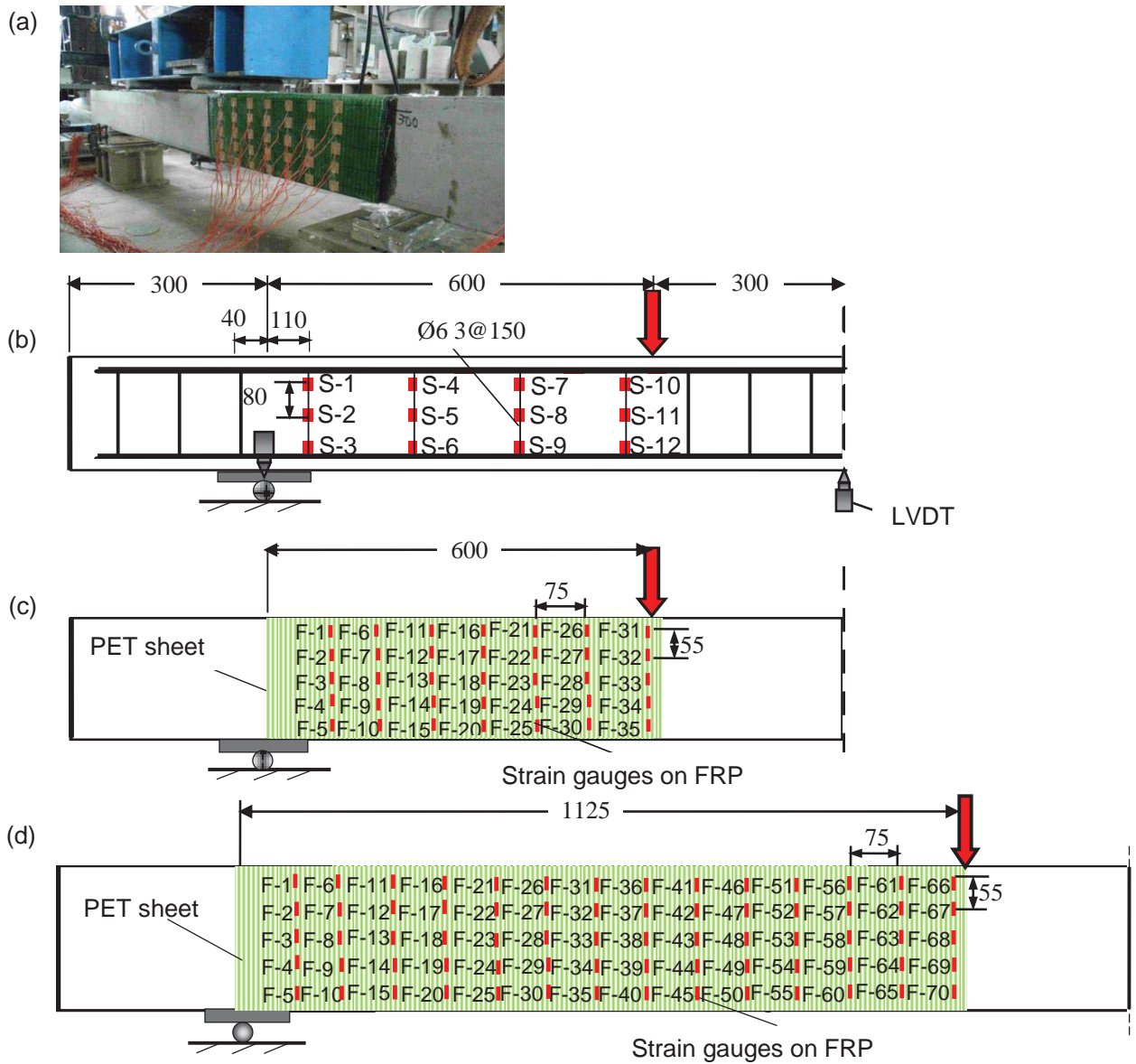


Fig. 2 Test setup: (a) asymmetrical loading; (b) locations of strain gauges on steel reinforcement; (c) locations of strain gauges on FRP (SP1-SP6, SP9); (d) locations of strain gauges on FRP (SP7)

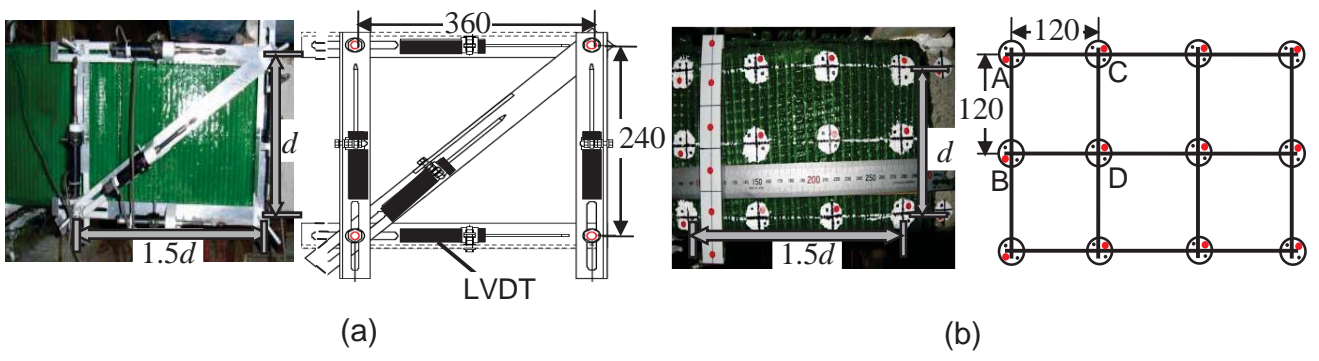


Fig. 3 Measurement of shear deformation: (a) Strain deformation measurement using LVDTs in SP1 to SP6; and (b) strain deformation measurement using image analysis in SP7 to SP10

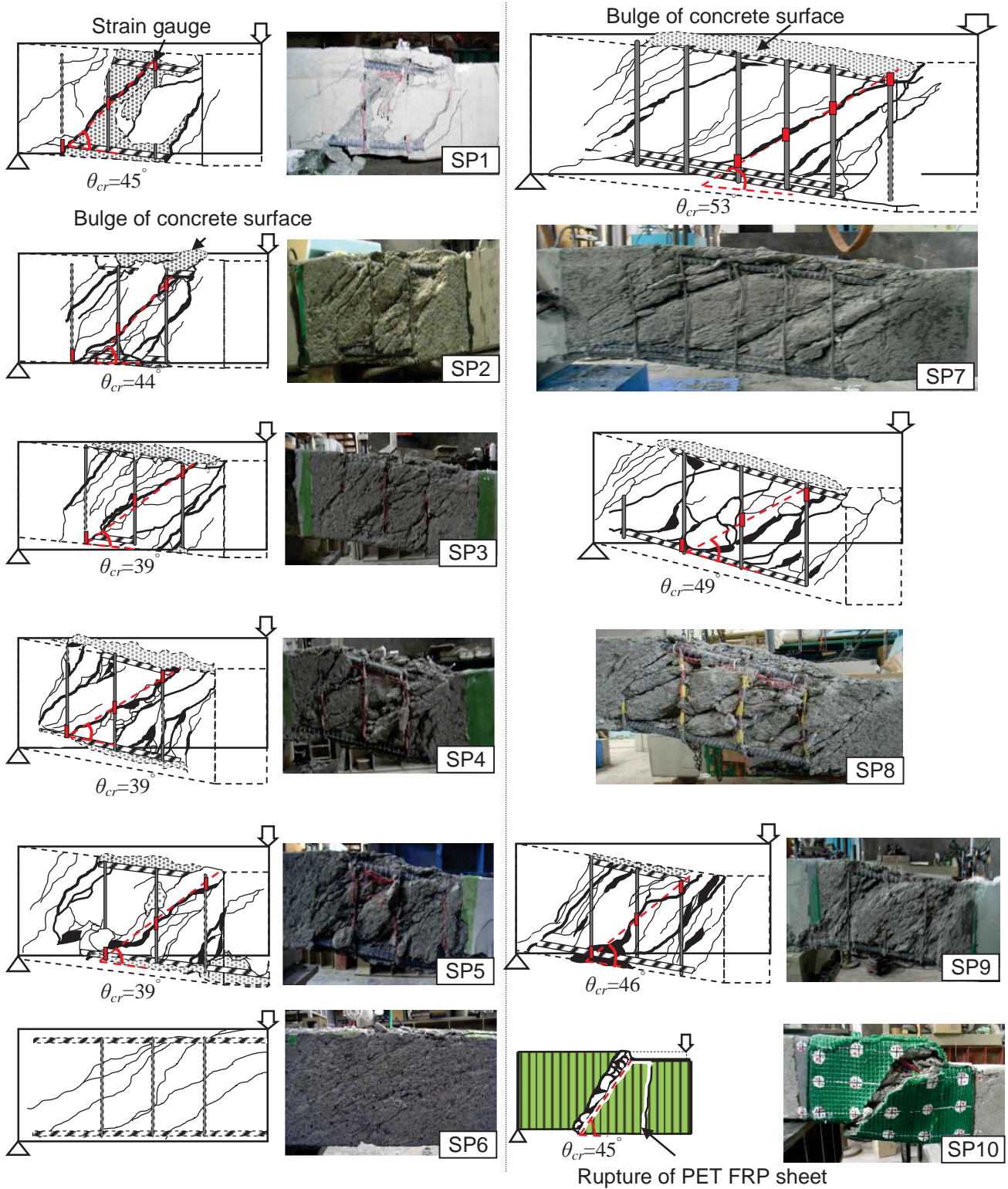


Fig. 4 Failure modes and crack patterns

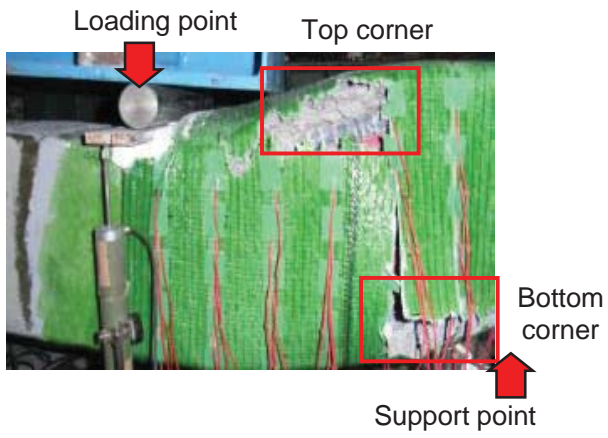


Fig. 5 Rupture and debonding location in PET sheet at termination of test in SP4

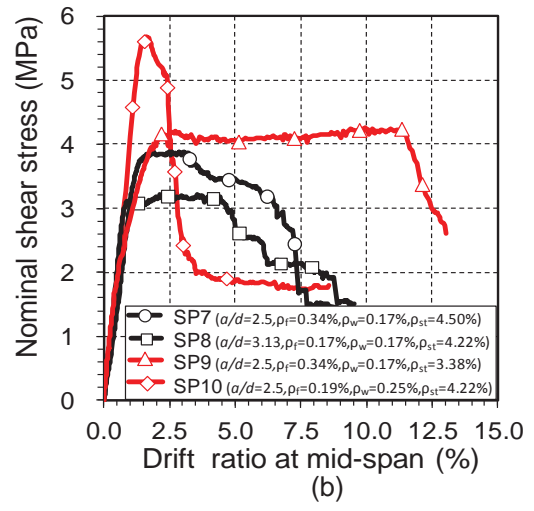
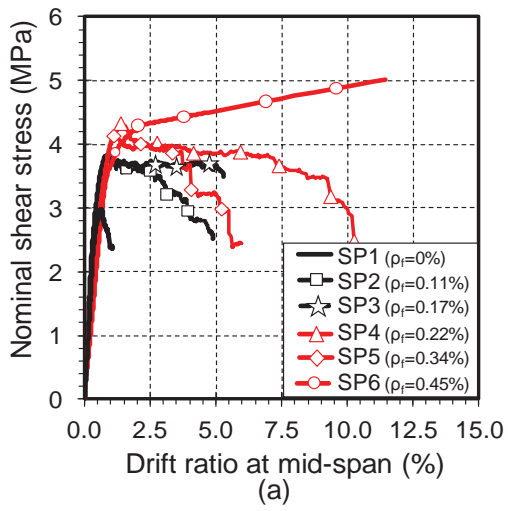


Fig. 6 Relationships between nominal shear stress (v) and drift ratio at mid-span (δ): (a) SP1 to SP6; and (b) SP7 to SP10

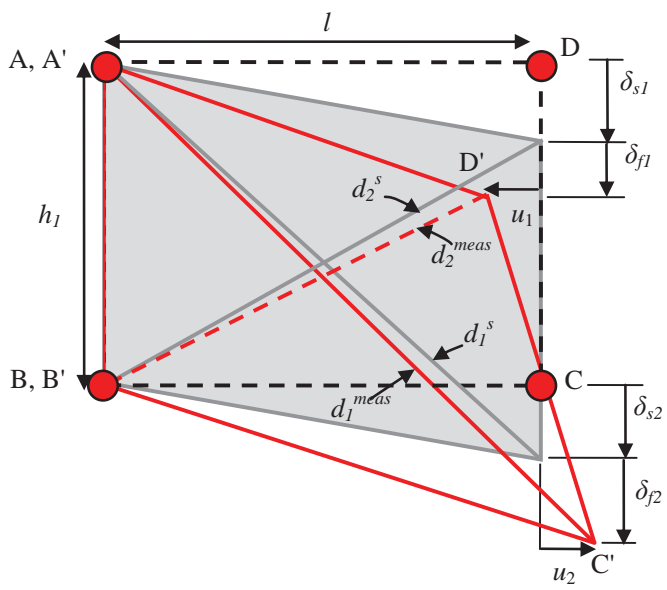
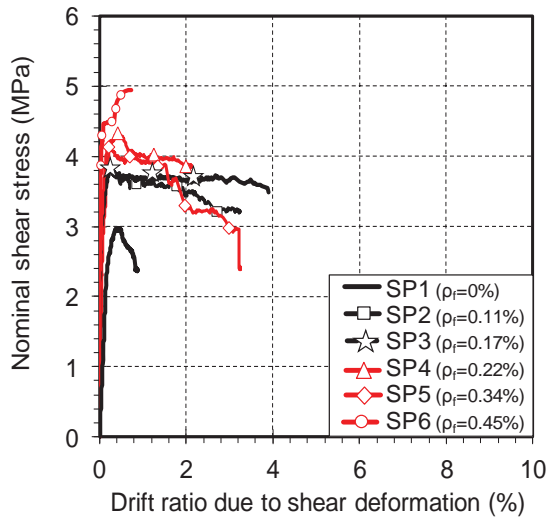
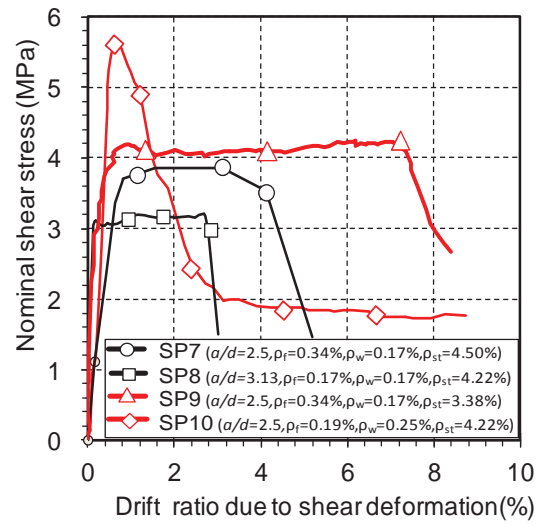


Fig. 7 Deformed configuration (Massone and Wallace 2004)



(a)



(b)

Fig. 8 Relationships between nominal shear stress (v_t) and drift ratio due to shear deformation at mid-span (δ_s): (a) SP1 to SP5; and (b) SP7 to SP10

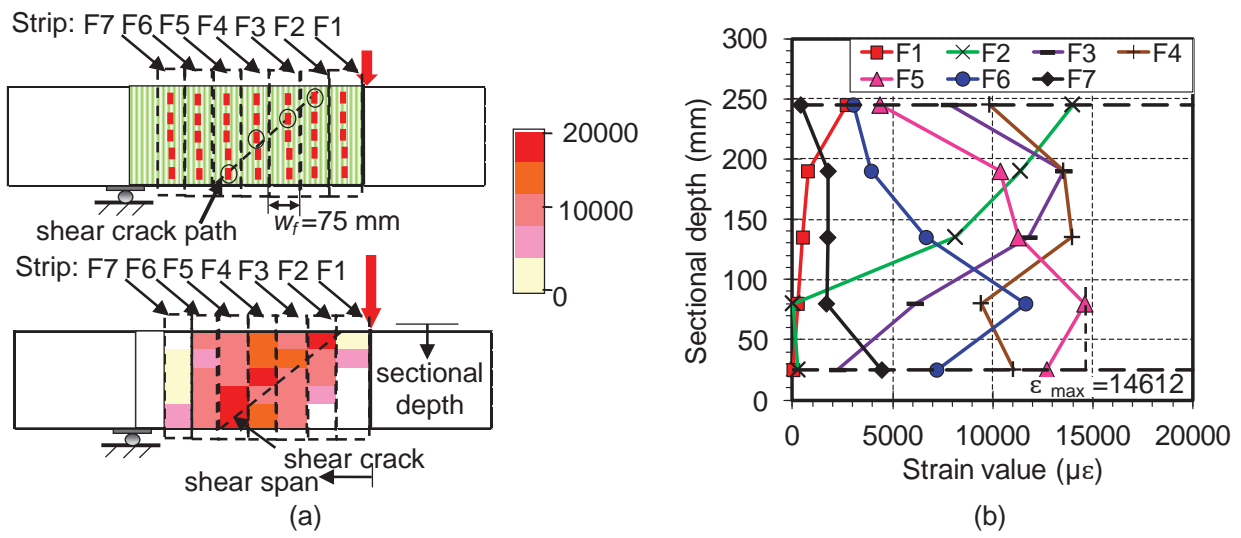


Fig. 9 Strain distribution of PET FRP sheet along the shear-span length at peak load: (a) strain of SP2 along shear-span; and (b) strain of SP2 along sectional depth

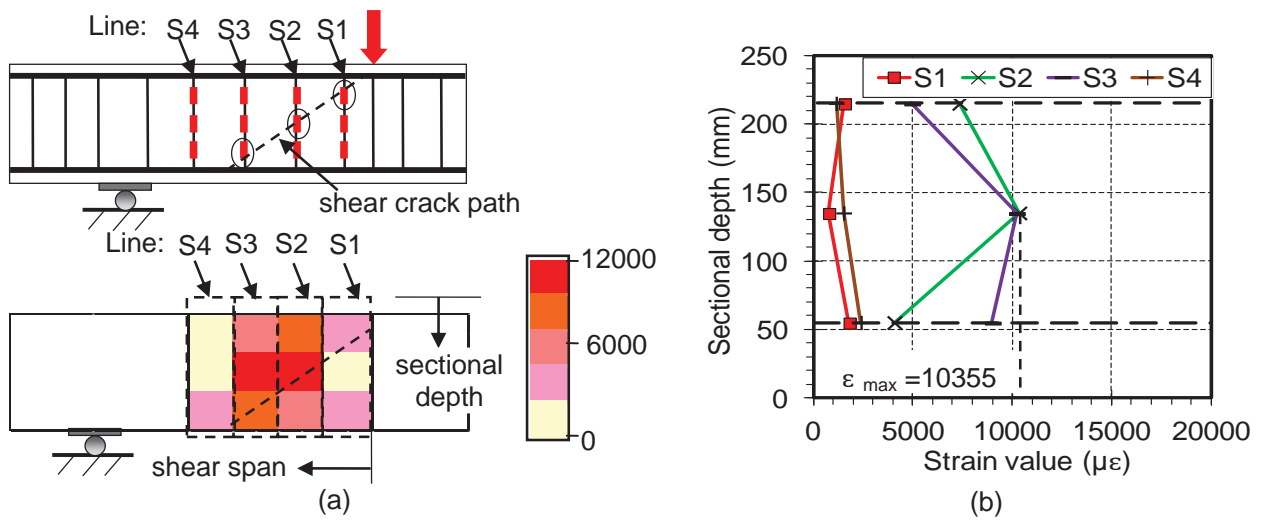


Fig. 10 Strain distribution of transverse steel reinforcement s along the shear-span length at peak load: (a) strain of SP2 along shear-span; and (b) strain of SP2 along sectional depth

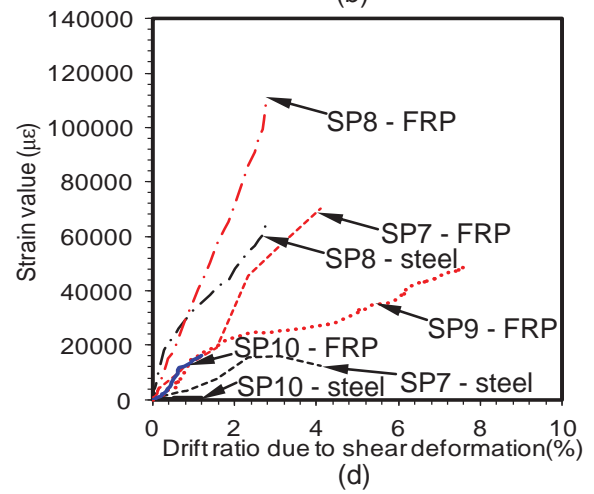
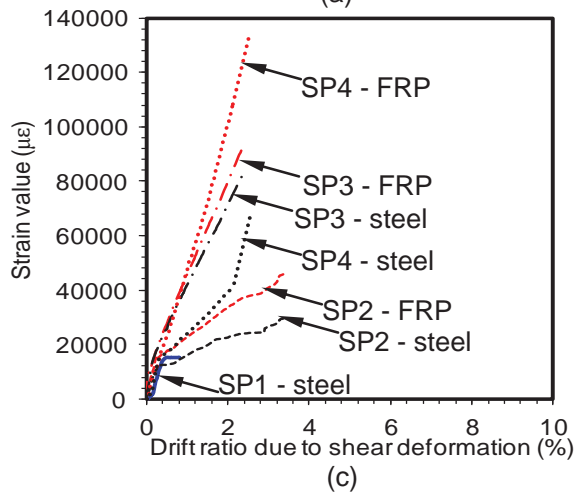
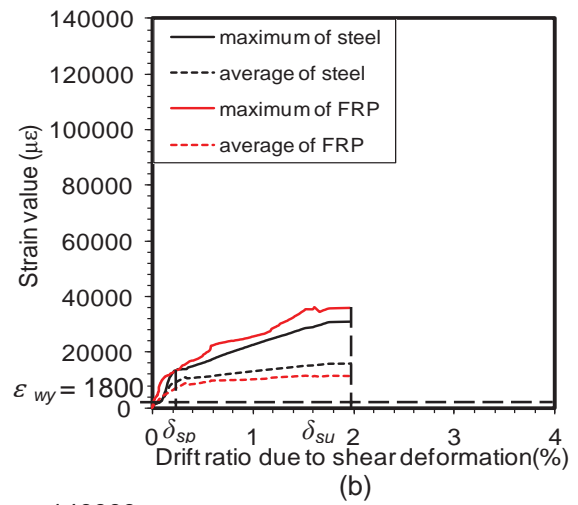
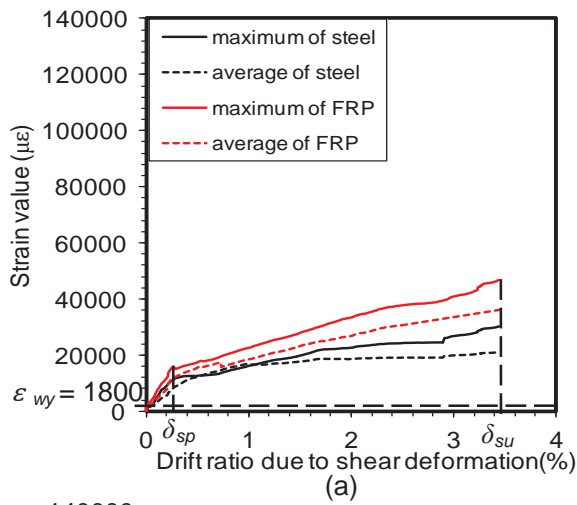


Fig. 11 Strain development of PET FRP sheet and steel reinforcement until ultimate deformation: (a) SP2; (b) SP5; (c) SP1 to SP4; and (d) SP7 to SP10

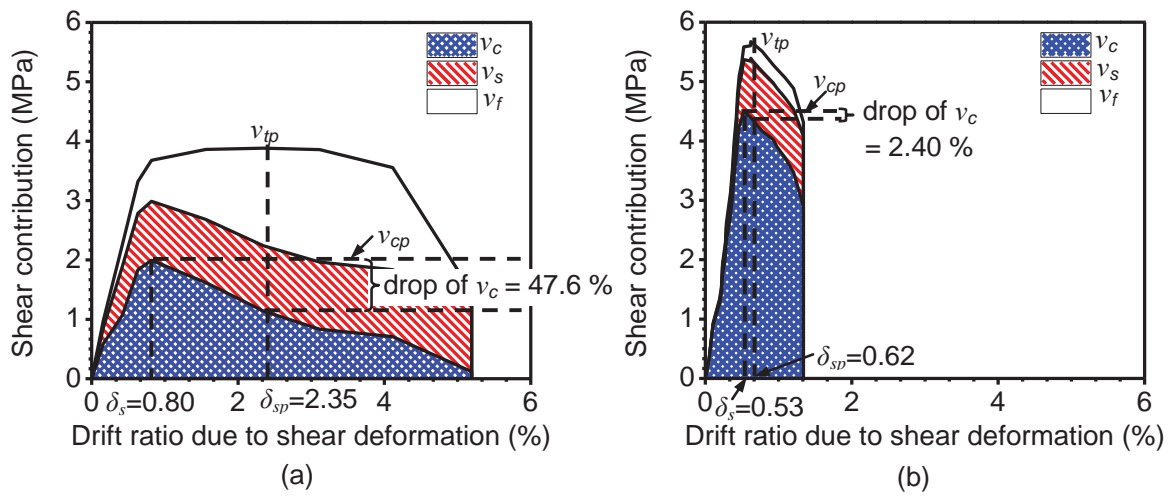
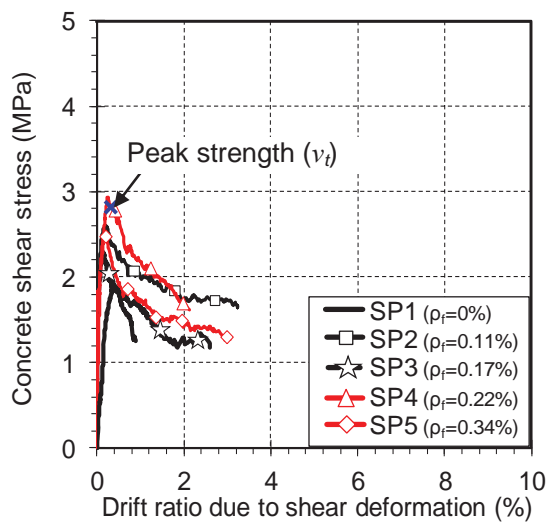
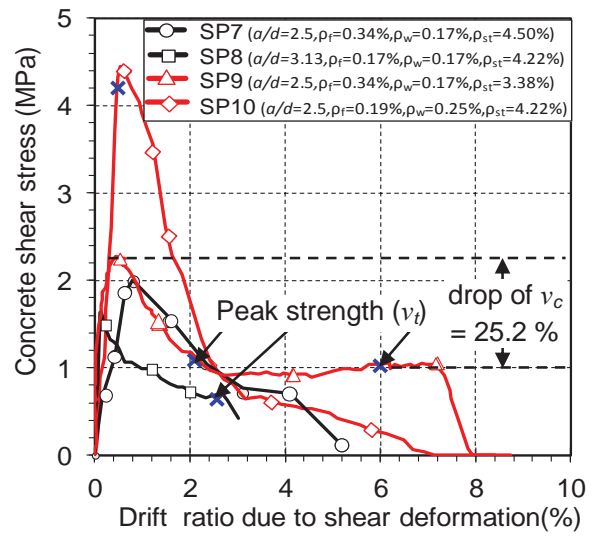


Fig. 12 Component of shear contribution: (a) SP7; and (b) SP10



(a)



(b)

Fig. 13 Relationships between concrete shear stress (v_c) and drift ratio due to shear deformation at mid-span (δ_s):

(a) SP1 to SP5; and (b) SP7 to SP10

List of Table Captions:

- Table 1 Details of test specimens
- Table 2 Material properties of steel reinforcement
- Table 3 Material properties of PET FRP sheets
- Table 4 Summary of test results in shear-stress and drift-ratio component
- Table 5 Strain development in PET FRP sheets and transverse steel reinforcement

List of figure captions:

- Fig. 1 Tensile test of flat coupon: (a) Tensile test and flat coupon; and (b) Stress-strain relationship of flat coupon
- Fig. 2 Test setup: (a) asymmetrical loading; (b) locations of strain gauges on steel reinforcement; (c) locations of strain gauges on FRP (SP1-SP6, SP9); (d) locations of strain gauges on FRP (SP7)
- Fig. 3 Measurement of shear deformation: (a) Strain deformation measurement using LVDTs in SP1 to SP6; and (b) strain deformation measurement using image analysis in SP7 to SP10
- Fig. 4 Failure modes and crack patterns
- Fig. 5 Rupture and debonding location in PET sheet at termination of test in SP4
- Fig. 6 Relationships between nominal shear stress (v) and drift ratio at mid-span (δ): (a) SP1 to SP6; and (b) SP7 to SP10
- Fig. 7 Deformed configuration (Massone and Wallace 2004)
- Fig. 8 Relationships between nominal shear stress (v_t) and drift ratio due to shear deformation at mid-span (δ_s): (a) SP1 to SP5; and (b) SP7 to SP10
- Fig. 9 Strain distribution of PET FRP sheet along the shear-span length at peak load: (a) strain of SP2 along shear-span; and (b) strain of SP2 along sectional depth
- Fig. 10 Strain distribution of transverse steel reinforcement s along the shear-span length at peak load: (a) strain of SP2 along shear-span; and (b) strain of SP2 along sectional depth
- Fig. 11 Strain development of PET FRP sheet and steel reinforcement until ultimate deformation: (a) SP2; (b) SP5; (c) SP1 to SP4; and (d) SP7 to SP10

Fig. 12 Component of shear contribution: (a) SP7; and (b) SP10

Fig. 13 Relationships between concrete shear stress (v_c) and drift ratio due to shear deformation at mid-span (δ_s): (a) SP1 to SP5; and (b) SP7 to SP10